Tellus (1990), *42A*, 230–245

Sensitivity of one-day predictions of meso-α and -β scales to model resolution

By MARINA ŽIVKOVIČ* and FERDINAND BAER, *Department of Meteorology, University of Maryland, College Park, Maryland 20742, USA*

(Manuscript received 7 June 1988; in final form 16 November 1988)

ABSTRACT

Recent studies of mesoscale predictability by operationally used limited-area models raise questions related to the implications of variance exchange between the scales which are resolved and which are not resolved by a variable model grid. In this paper, we demonstrate the rôle that model and initial data resolution plays in energy exchange between synoptic, meso-α, and meso-β scales. For that purpose, we consider 24-h evolution of barotropic channel flow on the β-plane. The number of modes investigated varies from 21 to 171 in the zonal direction and from 11 to 85 in the meridional direction. It is shown that dependence of nonlinear model interactions on spectral resolution varies with scales within the $k^{-5/3}$ mesoscale domain. A distinct region of scales in the meso-α and -β range is found to be insensitive, while surrounding modes are significantly affected by the choice of resolution. It is shown that the evolution of subsynoptic and meso-α modes depends upon variation of model resolution only, while the evolution of shortest meso-β modes is sensitive to variation of initial data resolution as well.

1. Introduction

Recent developments in enhanced sophistication of regional models bring into perspective the question of potential mesoscale model predictability. Models used for regional weather prediction are characterized by limited-area domains and resolution sufficient to resolve subsynoptic scales (Anthes, 1983). These scales have typical wavelengths of 200 km–2000 km and are often recognized as meso-α scales according to Orlanski's classification (1975). When their predictability by (utilizing) regional models is considered, one should note that the regional models provide different predictability results from the large-scale models. This was first noted by Anthes et al. (1985) during preliminary mesoscale predictability experiments when small or no error growth was observed.

Dissimilarity of error growth in global and regional models emphasize the importance of model nonlinearities and truncation as related to the use of limited area domains. The truncation of information from the large-scale is reflected in lateral boundary conditions, which are a major source of error in mesoscale models (Anthes, 1983). When combined with other sources of errors (initial conditions, parameterization, etc.) through nonlinear interaction, these boundary conditions determine the model error growth to be different than in global models.

Based on these considerations, it is becoming evident that nonlinear energy exchange between synoptic and meso-scales plays a crucial rôle in regional model predictability. As hypothesized by Anthes et al. (1985), the larger scales may determine almost exclusively the evolution of smaller scales resolved on the grids of regional models. However, given the models' complexities and strong case dependence, a significant research effort is required to confirm this hypothesis (e.g., Errico and Baumhefner, 1987).

* Presently affiliated with Department of Earth and Atmospheric Sciences at Purdue University, West Lafayette, Indiana 47907, USA.

In the present study, we will demonstrate some aspects of nonlinear interaction between synoptic and mesoscales. Our goal is to examine the sensitivity of this process to model resolution and to energy error variance present in the relevant scales of current regional models. For that purpose, we selected two simple nonlinear spectral models and utilized them in highly controlled numerical experiments; this choice helped to avoid the ambiguity inherent in complex models and real observations. We investigated the nonlinear interaction of as many as 171 zonal and 86 meridional modes by varying the model resolution from 100 km to 12.5 km. Our two models differed only insofar as one included localized forcing at the lower boundary and the other did not. Integrations of both models were monitored and compared during 24 hour forecasts.

The variable nature of mesoscale initial errors was simulated by designing initial data sets to deviate from a statistical $k^{-5/3}$ power law, and selection of the error scale was made by spectrally truncating data. The effect of orographic forcing on nonlinear variance exchange was obtained by comparison of the integration results from both models integrated with identical initial data.

The most interesting finding of the study is that a narrow band of meso-β scales (between 100 km and 200 km) plays an essential rôle in nonlinear energy exchange but does not allow error energy propagation from the shorter scales during a 24-h period. This result suggests that the predictability of meso-α scales may be fully controlled by the larger scales. It was also found that localized forcing influences predictability of the meso-α scales, but only marginally when compared to the impact of adequate model resolution.

In general, we will demonstrate how sensitivity of specific mesoscale modes to initial data and model truncation varies with scale when the initial energy distribution changes from a k^{-3} to a $k^{-5/3}$ power law. Our study illustrates how the dynamics of scale interactions is responsible for energy propagation in the region of meso-α scales and as such compensates in part for the gap existing between statistical-dynamical theory (e.g., Lorenz, 1969; Leith and Kraichnan, 1972) and predictability studies with operationally used mesoscale models.

2. Models

The nonlinear exchange of energy variance is the essential mechanism responsible for the development of spectral truncation error (in the sense of Merilees, 1972). While the rôle of spectral truncation error has been investigated for large-scale flows (e.g., Baer (1964) or Baer and Alyea (1971)), little is known about spectral truncation in the mesoscale. In order to investigate this error in relation to mesoscale predictability (referred to in the previous section), we utilize two models consisting of tendency and advection terms only and which conserve total system energy.

The two models used in this study are based upon the barotropic vorticity equation (BVE) and the potential vorticity equation (PVE) respectively. The BVE model is utilized to investigate the variation of solutions with changes of model truncation. Since the spectral truncation is varied over a range of mesoscale modes which may be sensitive to scale selection through forcing parameterization, an equivalent (PVE) barotropic model is also used. It provides additional information on the nonlinear interaction of mesoscale energy variance and constant mesoscale forcing at the lower boundary. Consistent scaling in both models ensures comparable model results.

The models are integrated for non-divergent channel flow on a mid-latitude β-plane. The basic channel length is assumed to be 4200 km and its width is 2100 km. With ψ denoting stream function, the governing equation for the first model is

$$\frac{\partial \nabla^2 \psi}{\partial t} = J(\nabla^2 \psi, \psi) + \beta \times \frac{\partial \psi}{\partial x}, \tag{2.1}$$

where the x-axis is oriented eastward and the y-axis is oriented northward, β is the Rossby parameter and J denotes the Jacobian operator. The additional assumption of a rigid fluid top is used when the governing equation for the second model (PVE) is derived;

$$\frac{\partial \nabla^2 \psi}{\partial t} = J(\nabla^2 \psi, \psi) + \beta \times \frac{\partial \psi}{\partial x} + f \times J(\ln H, \psi). \tag{2.2}$$

H is the equivalent fluid depth given by

$$H(x,y) = h(x,y) - h_o(x,y),$$

where $h(x,y)$ is a height of a fluid top and $h_0(x,y)$ is a perturbation amplitude at the fluid bottom.

Perturbation amplitude h_0 is described by a function which has two major properties; (i) it is highly localized and (ii) it meets the parity requirements of the spectral expansion functions. The first characteristic allows us to examine the influence of a constant flow perturbation at the lower boundary with the same wavelength as the shortest meso-α scale, i.e., 200 km. With necessary model resolution this forcing mechanism is represented more accurately by an increased number of grid points. The second property is necessitated by the lateral boundary conditions of the model. One possible function with such characteristics is

$$h_0(x,y) = \left\{1 - \exp\left(-\left(\sin\frac{2\pi x}{L2}\sin\frac{2\pi y}{L1}\right)^{445}\Big/ 4.45\right)\right\},$$

where L1 and L2 are domain dimensions in the meridional and the zonal directions respectively. Factors 445 and 4.45 provide necessary locality of the function which represents mesoscale peak on 200 km horizontal scale in the middle of domain. Function is given in nondimensional form and is projected onto a typical first internal mode.

The following scaling is applied to both models:

L	$\sim 10^6$ m	– length scale
$\lvert V\rvert$	~ 10 m s^{-1}	– horizontal velocity
T	$\sim 10^5$ s	– advective time scale
f	$\sim 10^{-4}$ s	– Coriolis parameter
β	$\sim 10^{-11}$ m^{-1} s^{-1}	– Rossby parameter
H	$\sim 3\cdot 10^3$ m	– fluid thickness

The fluid thickness H in the PVE model (2.2) is scaled by the equivalent depth of the first internal mode for the standard atmosphere. However, scaled perturbation amplitude h_0 is assumed to be 40% of that equivalent depth.

Both models are represented in spectral form by expanding the stream function into the series

$$\psi(x,y,t) = \sum_m \sum_n f_m^n(t)\,\psi_m^n(x,y), \quad \begin{matrix} -M \leqslant m \leqslant M \\ -N \leqslant n \leqslant N, \end{matrix} \tag{2.3}$$

and ψ_m^n are double Fourier expansion functions. Slip boundary conditions are implied in the meridional direction and periodic conditions in the zonal direction. Thus,

$$\psi_m^n(x,y) = \exp\left(i\frac{2\pi}{L2}mx\right)\sin\left(\frac{2\pi}{L1}ny\right). \tag{2.4}$$

Since ψ is a real function, the coefficients $f_m^n(t)$ are required to satisfy the following relationships:

$$\begin{aligned} f_m^{-n}(t) &= -f_m^n(t) \\ f_{-m}^n(t) &= -f_m^{n*}(t) \\ f_{-m}^{-n}(t) &= f_m^n(t), \end{aligned} \tag{2.5}$$

where the asterisk denotes complex conjugation.

With these conditions, $\psi(x,y,t)$ is completely specified by using the complex coefficients $f_m^n(t)$ for m and n in non-negative range, $m \geqslant 0$, $n \geqslant 0$. Constraints (2.5) reduce the number of needed unknown expansion coefficients by a factor of four, which in turn is reflected in sigificant reduction of computation time necessary for high resolution runs.

Nonlinear terms are evaluated on a grid by the pseudospectral technique (Orszag, 1970), and a centered second order finite difference scheme is used for time integration. The time step varies with change of resolution and is chosen to satisfy the CFL stability criterion formulated by Gottlieb and Orszag (1977). It is defined in nondimensional form to be

$$\Delta t \leqslant \frac{1}{2\pi(\mathrm{IQ}-1)}. \tag{2.6}$$

Where IQ is the largest number of collocation points in either direction for a chosen model resolution. Following Orszag (1971) only $\frac{2}{3}$ of the modes resolvable on the *collocation grid* are retained in our calculations in order to avoid aliasing errors. They are chosen to correspond to the spectral truncation limits listed in Table 1.

3. Numerical experiments

Our numerical experiments are designed to investigate three major questions: (i) how does model resolution and its associated spectral truncation affect nonlinear interaction on the mesoscale; (ii) how does the initial energy variance in the mesoscale effect this interaction; (iii) does the forcing at the lower boundary significantly alter mesoscale energy exchange?

Table 1. *Numerical characteristics of experiments showing relations between actual grid size, spectral truncation, shortest mesoscale resolvable on the grid, time step, and number of collocation points used for evaluation of nonlinear terms*

Grid size $\Delta x = \Delta y$	Grid code	Zonal wave nos.	Meridional wave nos.	Scale	Time step (Δ, t)	No. of collocation points zonal	meridional
100 km	C	20	10	α	30 min	64	32
50 km	M	42	21	α–β	15 min	128	64
25 km	F	84	42	β	7.5 min	256	128
12.5 km	FF	170	85	β	3.75 min	512	256

The first question is studied by integrating the BVE model (2.1) for various resolutions with the same initial data set. The second problem is examined by repeating this procedure for three different data sets. Finally, the third question is investigated by performing the same experiments described above but with the PVE model (2.2), thereby including localized mesoscale forcing at the lower boundary.

3.1. *Model resolution*

The technical essence of this study is to vary model and data resolution in such a manner that a wide range of modes are allowed to interact during time integration. This is accomplished by choosing a uniform grid whose size is varied by powers of two. Model spectral (and consequently scale) truncation is determined by the shortest waves resolvable on the grid in both the meridional and the zonal directions.

The coarsest model grid chosen consists of points with a separation of 100 km; given the overall dimensions this allows 20 waves to propagate in the zonal and 10 waves to propagate in the meridional direction (Table 1). Altogether 4 grids are used, and with halved intervals of the next most coarse grid; i.e., 100 km, 50 km, 25 km and 12.5 km. The grids are coded C, M, F and FF which stand for (C)oarse, (M)edium, (F)ine, and (F)ine-(F)ine grid, respectively. The same codes are used for corresponding spectral truncation. Thus, when the C grid is considered in the physical domain, its projection would be in the C modes of the spectral domain.

As the model grid size is varied, computational and scale characteristics are varied as listed in Table 1. The shortest meso-scales included by the model spectral truncation are given in the fifth column (Orlanski's classification (1975) is used). The number of collocation points and the time step required by the stability condition (2.6) are listed in the last three columns of the Table.

3.2. *Initial data sets*

Initial data are chosen to be compatible with model simulations of two-dimensional turbulence, yet to describe some observed features of atmospheric spectra. Thus, initial data sets are chosen such that the energy spectral coefficients describe a k^{-3} power law for synoptic wavelengths, and a $k^{-5/3}$ power law for mesoscale wavelengths (see curve (a) in Fig. 1). This choice is based upon statistical evidence of a k^{-3} power law enstrophy cascading range in large-scale atmospheric spectra (e.g., Fjørtoft, 1953; Leith, 1971; Charney, 1971). Gage (1979) also presented evidence for a $k^{-5/3}$ power law intertial range in mesoscale two-dimensional turbulence and many observations of horizontal wind spectra confirm this for wavelengths shorter than 1000 km (e.g., Lilly and Petersen, 1983)

Altogether three data sets are used; they are coded as FS00, FS12 and FS13 data and distribution of their energy spectral amplitudes are presented in Fig. 1. Diagram (a) shows the amplitude distribution given by Lilly and Petersen (1983), and which we used for our control data set (FS00 data). The spectral data set is completed by assigning identical amplitudes to all coefficients which are associated with each specified wave-vector. When projected onto a real two-dimensional domain (F grid) this data set represents channel flow with average winds of 2–3 m s^{-1} and a pronounced vortex as shown in Fig. 2. The coefficients' phases are chosen randomly.

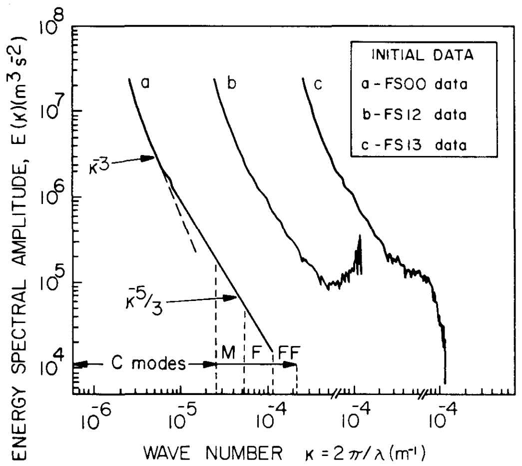

Fig. 1. Initial energy spectra of three: (a) FS00 data, (b) FS12 data, and (c) FS13 data. Distribution curve (a) corresponds to results of Lilly and Petersen (1983), and is used for control model runs. Diagram curves (b) and (c) represent two possible deviations from FS00 spectrum due to mesoscale perturbation. Marks C, M, F and FF denote the wavenumbers that correspond to spectral truncation limits of different size grids (Table 1).

The other data sets, FS12 and FS13, (curves (b) and (c) in Fig. 1, respectively) are chosen to deviate from the statistical law in the mesoscale region as follows. The stream function field given by the FS00 data set (Fig. 2) is perturbed at one point common to all of the grids. This perturbation is determined by reducing the stream function value at one point in the vicinity of the second vortex maxima (near the west boundary shown in Fig. 2) to half its original value. The stream function field with this perturbation is transformed back into F spectral domain, and results in a white noise spectra which is added to the wavelengths shorter than 200 km (curve (b) in Fig. 1). This new set of spectral coefficients values is called the FS12 data set. It represents spectrum deviation caused by an arbitrary initial value at a point common to any size grid.

This kind of perturbation may be interpreted in one of two ways: either it is equivalent to an observational error which exists at one point of any size grid or it is equivalent to an error due to insufficient resolution. In the latter case, the error would not exist if higher data resolution were used, and could be due to the existence of sub-C-grid mesoscale structure. We describe one such structure by data set FS13 (curve (c) in Fig. 1). It is created by a similar transformation of the FS00 stream field to the FS12 data set. In addition, however, the perturbation is linearly interpolated to the twelve neighbouring points on the F grid which do not exist on the C grid. Thus, the FS13 data set includes perturbation amplitudes of the same value as in the FS12 data set but also describes a structured sub-C-grid scale phenomenon.

As summarized in Fig. 1, all three data sets describe same power law for synoptic wavenumbers marked as the C modes on curve (a). The other two curves (b) and (c) have the same slope in the C wavenumber region (note displaced abscissa for these two curves). In the mesoscale region, however, two curves show significant deviation from the $k^{-5/3}$ power law.

The wavenumber limits corresponding to the C, M, F, and FF grids from Table 1 are also marked on Fig. 1. Depending on the model run, spectral coefficients are initialized with values given by the chosen energy distribution curve within each of the marked wavenumber ranges. Hence, if the model simulates flow on the C grid

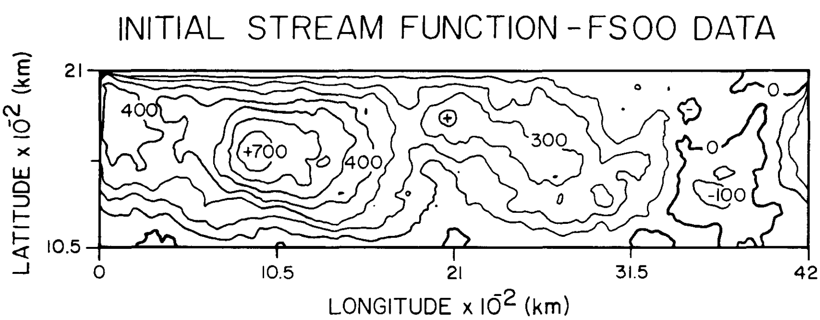

Fig. 2. The stream function field derived from the FS00 data with randomly chosen phases.

only, C initial coefficients are used. Similarly, only M initial coefficients are used for the M model grid and F coefficients for the F grid. (Note that all coefficients between the F and FF marks are always set to zero.) We define "data truncation" limits according to the previous wavenumber specification. Thus, if the C initial coefficients are assigned nonzero values from any of the data sets, we call this "the C data truncation", and if the M, F or FF coefficients are required by the choice of model grid ("model truncation") they are assigned zero values initially. According to this definition the highest data truncation is F and the highest model truncation is FF. Possible combinations of model and data truncations used in the present study are listed in the last column of Table 2.

3.3. Organization of numerical experiments

The results presented here are obtained from 53 numerical integrations organized into nine experiments. Each of the experiments consists of

Table 2. *List of the experiments and initial data used. The model and data truncation (last column) were coded as listed in Table 1*

Experiment no.	Case title and code	Model type	Initial data set	Truncation: model	Truncation: data			
1.	control case, (CC)	BVE	FS00	C	C			
				M	C	M		
				F	C	M	F	
				FF	C	M	F	FF
2.	error 2 case, (ER2)	BVE	FS12	C	C			
				M	C	M		
				F	C	M	F	
				FF	C	M	F	FF
3.	error 3 case, (ER3)	BVE	FS13	C	C			
				M	C	M		
				F	C	M	F	
				FF	C	M	F	FF
4.	topography case, (TC)	PVE	FS00	C	C			
				M	C	M		
				F	C	M	F	
5.	error 4 case, (ER4)	PVE	FS12	C	C			
				M	C	M		
				F	C	M	F	
6.	error 5 case, (ER5)	PVE	FS13	C	C			
				M	C	M		
				F	C	M	F	
7.	scaled control case	BVE	FS00	C	C			
				M	C			
				F			F	
				FF			F	
8.	topography case with 10% perturbation	PVE	FS00	C	C			
				M	C			
9.	topography case with 90% perturbation	PVE	FS00	C	C			
				M	C			

a number of integrations classified according to the choice of initial data and model type (BVE or PVE). They are summarized in Table 2.

In the first 3 experiments, the BVE model is integrated for each of 3 data sets: FS00, FS12, and FS13. The experiment nos. 4, 5 and 6 are identical with the first 3 except that the PVE model is integrated. The last 3 experiments are basically designed as needed to complement the results of the first six experiments. Thus, the "scaled control case" consists of runs of the BVE model with two orders of magnitude smaller "β-term" providing results on the influence of the Coriolis force in the integrations. Similarly, the effect of the perturbation amplitude at the lower boundary is examined in more detail in the eighth and the ninth experiments with assumed 10% and 90% perturbation amplitude, respectively.

Each numerical integration within any experiment is uniquely defined for specific model and data scale truncation. Depending on the model run, spectral coefficients are initialized with nonzero values given by the energy distribution curve within each marked wavenumber range from Fig. 1. For example, the first experiment called Control Case (CC) is composed of ten numerical runs initialized with FS00 data for different model and data truncation (Table 2). Thus, the integration with the C model truncation is done using only C nonzero initial amplitudes. Integrations with the M model truncation, however, include two runs: one with the C data truncation and one with the M data truncation, etc. This procedure enables comparison of the model resolution impact for identical initial data. It also helps to determine the importance of finely gridded initial information on the final forecast.

4. Results

We review our results in three separated categories: (i) as a function of model resolution, (ii) as a function of data (initial condition) resolution, and (iii) as a function of the forcing at the lower boundary. It will be shown that those waves which include subsynoptic and longer meso-α waves are sensitive only to the choice of model resolution. Towards the shorter scales, the mesoscale modes are virtually insensitive to variation in both model and data resolution. Finally, the shortest modes investigated are found to be sensitive not only to model resolution but also to the truncation of small-scale energy variance. Integrations with the PVE model reveal that only the C modes can be affected by a chosen perturbation at the lower boundary.

4.1. Sensitivity of prediction to model resolution

A comparison of predictions obtained for different model resolutions but using the same initial conditions illustrates the sensitivity of those integrations to the variation in model resolution. For example, in the first experiment (Table 2) the four runs with the C, M, F and FF model grids are compared uising the same C data truncation; the three runs M, F and FF are compared for the same M data truncation and the two runs F and FF are compared for the same F data truncation all with the FS00 data set. The observations described below are determined by applying this procedure to the results of the first 6 experiments.

4.1.1. The C modes. The comparison of runs is made by calculating relative differences between coefficient amplitudes predicted on different model grids. Fig. 3 is an example of the relative difference map in predicted amplitudes of the C modes after 24 h. The characters **C** and **F** in the difference formulation, (Fc − Cc)/Cc, represent model truncation, and the smaller character c denotes data truncation used in the runs being

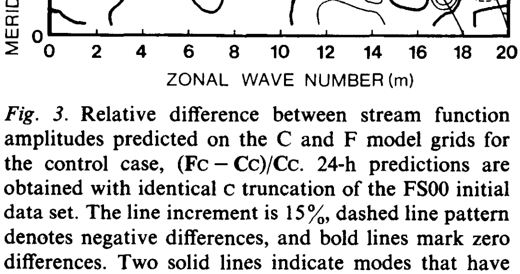

Fig. 3. Relative difference between stream function amplitudes predicted on the C and F model grids for the control case, (Fc − Cc)/Cc. 24-h predictions are obtained with identical c truncation of the FS00 initial data set. The line increment is 15%, dashed line pattern denotes negative differences, and bold lines mark zero differences. Two solid lines indicate modes that have the same amplitude initially.

compared. This difference diagram is presented in the two-dimensional wavenumber domain with the dashed line pattern denoting negative values. The contour interval is 15%.

Distinct regions of extreme differences are noticeable in this diagram. For example, mode $m = 19$, $n = 6$ has over 60% more amplitude when predicted on the finer F grid as compared to the C grid prediction. Alternatively, mode $m = 18$, $n = 5$ has 35% more amplitude when predicted on the C grid than on the F grid. At first sight this difference diagram does not seem to show a regular pattern of positive and negative values. However, the 2 solid lines on the diagram connect modes which represent wave-vectors with the same initial amplitude. Along these lines, it is evident that differences tend to alter sign for neighbouring wave-vectors. This suggests that the difference in predictions is due, at least in part, to truncation constrained nonlinear exchange of amplitude on the C grid. Almost identical difference diagrams are obtained when the C grid integrations are compared to the M or the FF grid integrations.

Comparison of energy distributions obtained for integrations on the C and M grids (Fig. 4) confirms this observation. Considering the time scale of our integrations and the model's energy

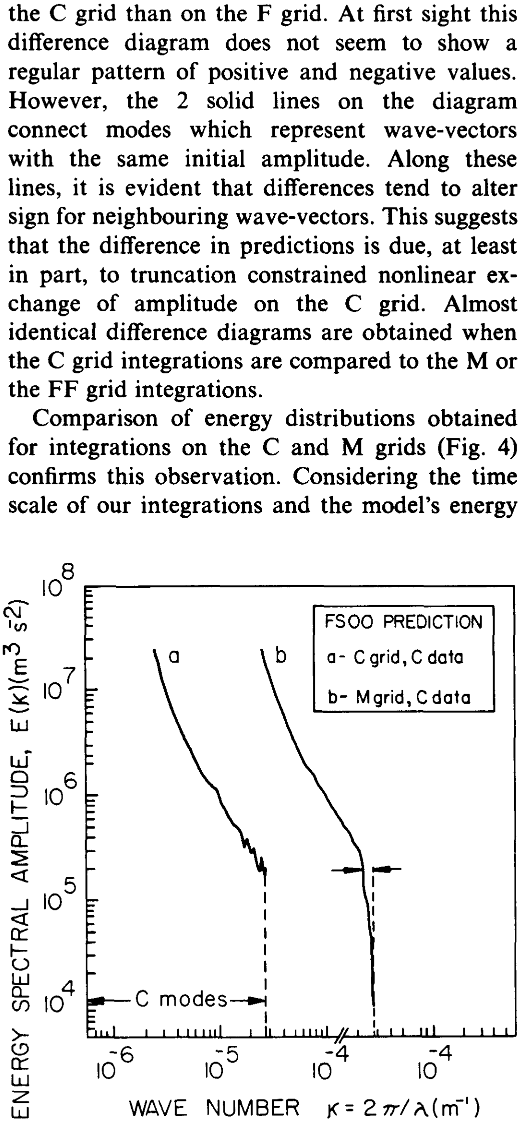

Fig. 4. 24-h energy distribution predicted on (a) the C grid and (b) the M grid for the control case.

conserving property (no source or sink of energy exists), the final energy distributions should be similar to the initial ones. Indeed, the 2 curves on Fig. 4 show identical distributions for the longest waves. But the modes closer to the C truncation limit show different final values on the 2 grids. The uneven shape of curve (a) suggests unrealistic accumulation of energy in the shortest modes. When the integration is performed on the M model grid, the energy curve (b) becomes smooth although the sharp drop of energy occurs due to zero initial values of the M modes. These results suggest that increased model resolution M is more suitable for the nonlinear interaction of the shortest C modes.

The phenomenon described above is called "spectral blocking" by Machenhauer (1979) and is caused by an accumulation of amplitude in the shortest spectral components due to truncation by the model nonlinear operators. We note this result as fictitious amplitude prediction on the C grid. If accumulated energy is not "diffused" by subgrid scale parameterization it will result in a spectral truncation error. An increase in resolution (the M grid has twice the resolution of the C grid) seems to avoid this error although further increases in resolution do not cause significant additional improvement. This latter observation is best illustrated by the time evolution of the most variable modes seen in Fig. 3. The evolution of amplitude of the 2 such modes from the control case experiment (the 1st experiment in Table 2) is shown in Fig. 5. It is apparent that the major difference appears between the C and M grid integrations (dashed and broken line patterns, respectively). Results for the F and FF grids follow almost the same evolution as those calculated on the M grid.

4.1.2. The M modes. The M modes exhibit a different sensitivity pattern from the C modes when model resolution is increased. There is virtually no difference between the runs on the M or the F model grid when only M modes are initialized (differences $(F_M - M_M)/M_M$ are almost zero). The energy distribution curves obtained from the predictions of the M modes confirms this observation. In Fig. 6 3 predicted energy distribution curves are presented: for the C modes, for the M modes and for the F modes. The smooth pattern of curve (b) (the M modes) does not suggest presence of any accumulation of spectral ampli-

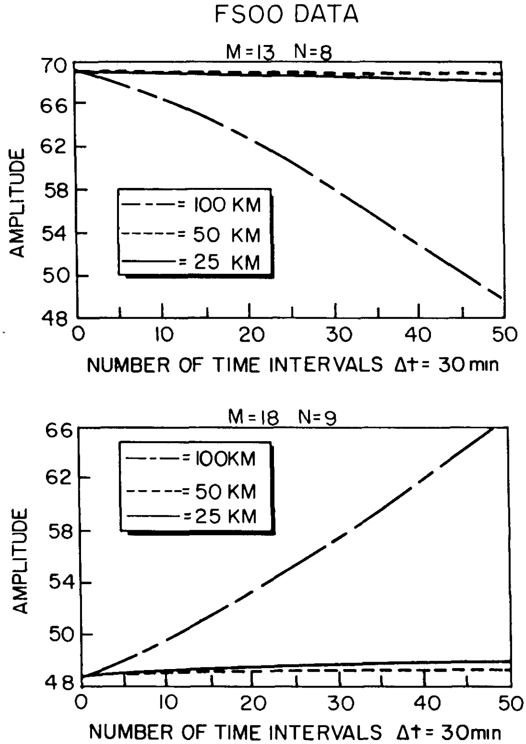

Fig. 5. 24-h amplitude evolution of two modes from Fig. 3 predicted on 3 model grids: C, M and F. The most varying curve in each of the diagrams represents prediction on the C grid (100 km grid size). Time interval is 30 min.

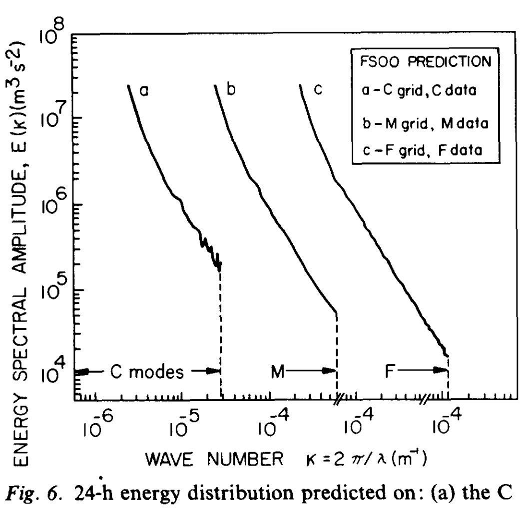

Fig. 6. 24-h energy distribution predicted on: (a) the C grid using C data truncation; (b) the M grid using M data truncation; (c) the F grid using the F data truncation in the control case.

tude when compared to the curves for C and F modes. This result implies that the evolution of the M modes during 24-h time period is dominated significantly by the energy of the long C modes hence further increase of the model resolution does not effect their 24-h evolution.

4.1.3. The F modes. When the F modes are considered (curve (c) in Fig. 6) the accumulation of spectral amplitudes reappears. Indeed, when the runs on **F** and **FF** grids are compared, differences **(FF − F)/F** in predictions become noticeable (Fig. 7). The relative differences given on Fig. 7a for the case of the FS00 data indicate that the shorter F modes are sensitive to the choice of resolution although not to the same extent as the C modes in Fig. 3. Indeed, energy distribution curves (a) and (b) in Fig. 8 for the F and FF model truncations respectively, are very similar to the corresponding curves on Fig. 4 for the C modes.

Use of the FS12 or FS13 data emphasizes this senstivity of the F modes (Figs. 7b, c). When amplitudes of the higher M modes and lower F modes deviate from $k^{-5/3}$ power law the relative differences in the predictions substantially exceed the differences for the FS00 data showing that the F modes are very sensitive to the scale truncation error and related truncation of the energy variance exchange. The dependence of their forecast on the energy structure in the F-mode region is highlighted on Fig. 9. In this diagram, we describe the time evolution during the forecast of the root mean square (RMS) amplitude difference of all the F modes for the model which includes the FF modes as compared to the model without these modes. The results are surprisingly sensitive to the initial energy distribution of the F modes. It appears that the forecast is considerably more sensitive to resolution in the model for those initial distributions in which the short scale energy decays with scale (FS00 and FS13 data). Conversely, if the erroneous energy in the initial state is present in the shortest scale, as is seen in the FS12 case, the integrations seem insensitive to additional model resolution.

Thus we may draw the following tentative conclusion. If a local pulse focused on the smallest model scale can be resolved on the grid, expanding the model resolution will not necessarily improve the forecast. On the other hand,

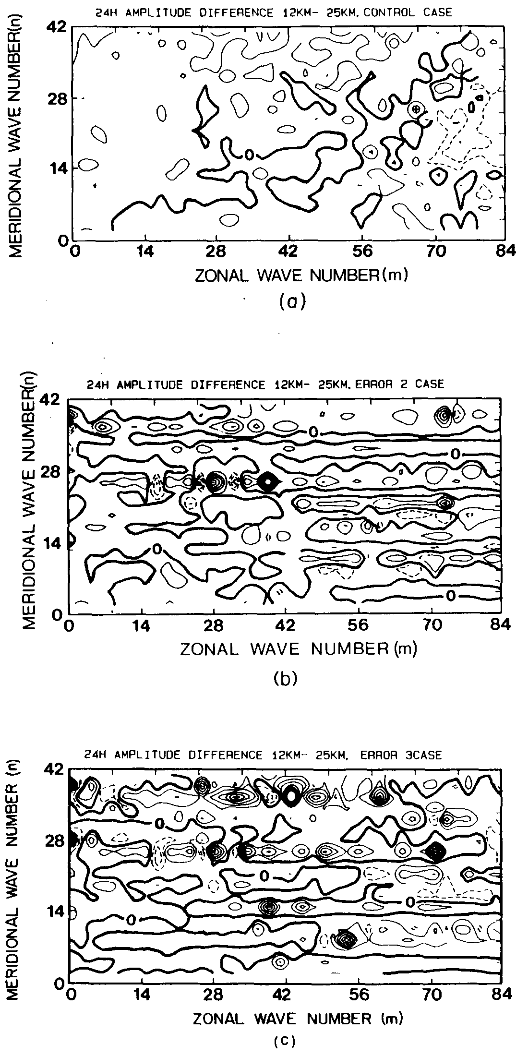

Fig. 7. Relative difference between stream function amplitudes predicted on the F and FF model grids, (FF − F)/F. 24-h predictions are obtained for: (a) FS00 data, (b) FS12 data, and FS13 data. The line increment is 15%, dashed line pattern denotes negative differences, and bold lines denote zero differences. Differences between predicted amplitudes exceed 100% for some of the F modes.

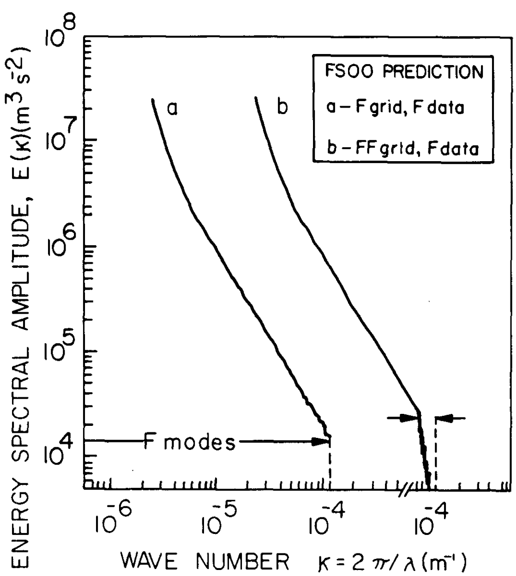

Fig. 8. 24-h energy distribution predicted on (a) the F grid and (b) the FF grid in the control case.

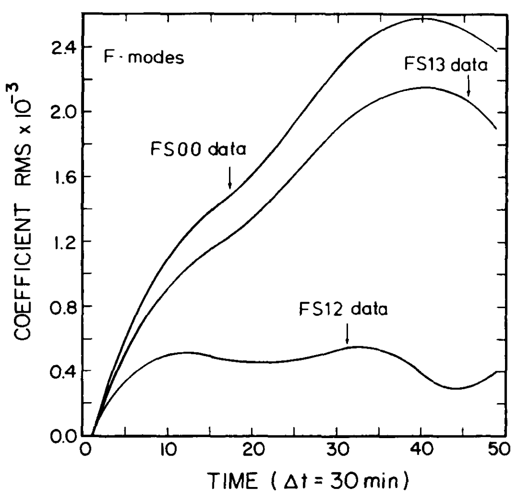

Fig. 9. The evolution of RMS stream function amplitude differences of the F modes for each of three data sets: FS00, FS12, and FS13. The integrations which include the FF modes are compared to the model integrations without FF modes in the control case, error 2 case and error 3 case.

if the local pulse is smoothed over many small scales so that the energy decreases with decreasing scale, expanding the grid will yield a modified solution on integration.

4.1.4. The C, M and F modes. The results discussed above are summarized in Fig. 10 as obtained in the Control Case Experiment. It represents the evolution of RMS amplitude differences for each of the mode ranges, i.e., the C,

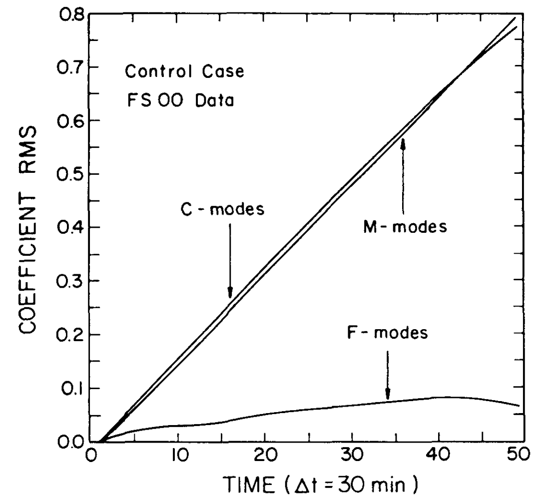

Fig. 10. The evolution of RMS stream function amplitude differences for each mode range C, M, and F, as obtained from the control case experiment. Similar diagrams are obtained in the error 2 and error 3 cases.

M, and F ranges. The RMS differences are calculated between the model amplitudes predicted on two model grids using identical initial data. For example, the RMS differences in the M modes were determined from the predictions on the M and F model grids. In both model runs the M modes had the same initial values, and the F modes required by the F model grid were assigned zero initial values. Similarly, the differences in the C and the F modes were calculated between the predictions obtained on the C and M model grids, and the F and FF model grids, respectively.

The RMS differences in the C modes predictions increase almost linearly in time as indicated by the uppermost curve in the diagram. Predicted amplitudes of the M modes resemble very closely the evolution curve of the C modes. However, RMS difference evolution of the F modes (the lowest curve in diagram) shows a different pattern and has one order of magnitude smaller values. The closeness of the C and M modes' evolution curves confirms our finding that the M modes predictions are controlled by the energy of the C modes on the 24-h time scale. Over the same time period the F modes, however, do not show dependence upon the C modes amplitudes.

This general observation was also supported by integrations with the PVE model (topography case, error 4 and error 5 experiments) and is independent of the choice of initial energy distribution (as shown by the error 2 and error 3 experiments). Thus, one can conclude that the shorter meso-β scales (the F modes) are not influenced by the energy in the longer scales during a 24-h interval, but they are sensitive to model resolution and energy variance present in the surrounding scales.

4.2. *Sensitivity of prediction to data resolution*

The findings reviewed above suggest that truncation error depends upon the modal energy distribution in the vicinity of model truncation limits. This will be confirmed by results to follow based upon the model integrations with various data truncation (see Subsection 3.3). We will compare the predictions obtained for different model resolutions for the same data set but for different data truncation. Thus, for example, in the 1st experiment runs on the C grid with C mode initialization will be compared with M runs with M mode initialization. The resulting difference diagrams are compared with the ones from Subsection 4.1.

4.2.1. *The C modes.* As shown above, to ensure adequate prediction of the C modes, it was necessary to use at least the M model truncation, corresponding to a 50 km horizontal resolution. One may then ask whether it is also necessary to have nonvanishing initial conditions for all required M modes. The answer is obtained by comparing the C and M model predictions with and without initial energy in the additional M modes for the first 6 experiments. Relative differences in predicted amplitudes $(M_C - C_C)/C_C$ and $(M_M - C_C)/C_C$ (of a type given on Fig. 3) are calculated and compared. The same procedure is also used for the F grid; $(F_C - C_C)/C_C$ and $(F_F - C_C)/C_C$ diagrams are compared.

All of the diagrams show one common feature, i.e., there is virtually no difference when additional M or F modes are initialized. Therefore, we can conclude that for the correct prediction of the C modes, at least for 24 h, higher M modes are needed but not the detailed information on their initial structure.

4.2.2. *The M modes.* Similar comparison of the integrations on the M and F grids with the M and

F data [(FM − MM)/MM and (FF − MM)/MM] truncation suggests a different sensitivity of the M modes to the truncation of initial F modes. As already described in Subsection 4.1.2, the M modes are virtually insensitive to an increase of model resolution (the F grid) for all three data sets when only M modes are initialized. However, when nonvanishing initial F modes are included a slight difference appears, especially in the case of FS12 and FS13 data. It is noticeable on Fig. 11 that predicted values can differ by 5–45% when initial F scale values are included in the calculations.

It is also noticeable on Fig. 11a that differences are of the opposite sign from the differences in diagram (b). Diagram 11a represents the results for FS12 data and indicates generally larger predicted values with the F modes being initialized. Diagram 11b is based on calculations with the FS13 data and shows generally smaller values of predicted amplitudes (negative differences) when non-zero values of the F modes are used. This different response reflects the difference between 2 data sets. In the case of FS12, the neighbouring F modes have comparably higher amplitudes than the longer M modes, whereas in FS13 the F modes have significantly lower relative values. Thus, positive differences in the first case indicate that the rôle of the model grid resolution is reinforced by the inclusion of erroneous energy in the shortest modes. Negative differences in the latter case, however, indicate that the rôle of initial conditions counteracts the rôle of model grid truncation.

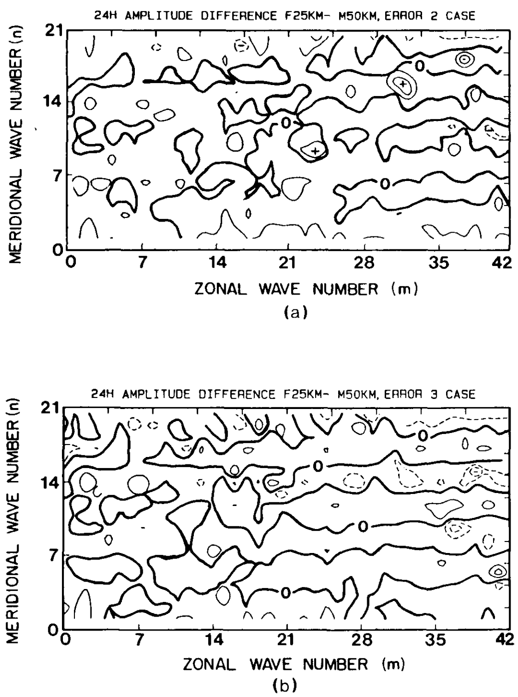

Fig. 11. Relative difference between stream function amplitudes predicted on the M and F grids, (FF − MM)/MM, in (a) error 2 case and (b) error 3 case. The M truncation of initial data is used for integrations on the M model grid and the F truncation of initial data is used for integrations on the F grid. The line increment is 15%, dashed line pattern denotes negative differences, and bold lines mark zero differences.

4.2.3. The F modes. A procedure similar to the one used above could not be applied for the F modes, since the additional FF modes are always assumed to be zero initially. However, the impact of their involvement in integrations with 3 different data sets (Fig. 7) provides evidence that their predictability is strongly related to energy variance present in those scales. Thus it is to be expected that these modes will be even more sensitive to inclusion of the initial information on the FF scales.

4.3. *Sensitivity of prediction to perturbation of the lower boundary*

Experiment nos. 4, 5, and 6 (topography case, error 4 case and error 5 case in Table 2) consist of integrations of the PVE model and include a constant perturbation at the lower boundary. The perturbation amplitude at the lower boundary in these experiments is assumed to be 40% of the equivalent depth. In order to isolate the sensitivity of the solution to perturbation amplitude, two additional experiments are made (numbers eight and nine in Table 2). When the runs from these 5 experiments are compared with corresponding runs of the BVE model it is noted that *only* the C modes are affected by forcing.

The diagrams on Fig. 12 illustrate this comparison of the C modes predictions obtained in integrations of the BVE and PVE models using FS00 initial data. Relative differences in predicted amplitudes between the integrations with the C model and C data truncation are calculated. Differences between the PVE model inte-

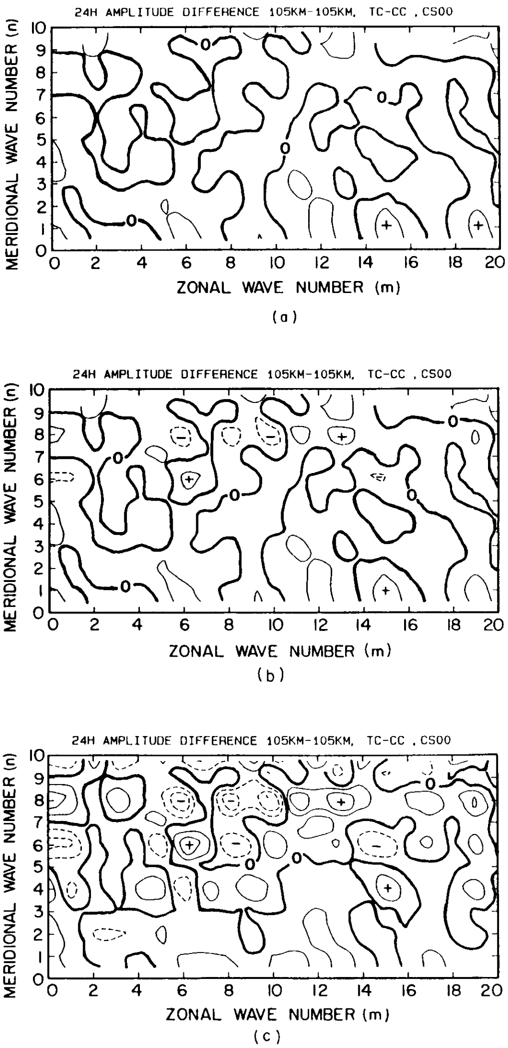

Fig. 12. Relative differences between stream function amplitudes of the C modes predicted by the BVE and PVE models using identical initial data (FS00). Integrations of the PVE model included (a) 10%; (b) 40%; (c) 90% perturbation amplitude. The line increment is 15%, dashed line pattern denotes negative differences, and bold lines mark zero differences.

gration with 10% perturbation and the BVE model are shown in diagram (a). Diagrams (b) and (c) represent results PVE model with 40 and 90% perturbation, respectively.

It is noted that in case (a) small differences between runs exists (modes $m = 17$, $n = 1$, 2) while in case (c) differences reach values of 30% and more. Diagram (b) indicates that only some of the C modes are affected, and indeed these are the modes that exhibit increased sensitivity to model resolution. This observation holds even when different initial data sets are used, i.e., the FS12 and FS13 data, which means that our forcing simulations increase the sensitivity of the C modes independently of energy distribution in the shorter mesoscale. Scale selective nature of the solution sensitivity to perturbation at the lower boundary is suggestive of the influence of model formulation on these results which can dominate over the results sensitivity to scale truncation. Indeed, the rotational term in the PVE coupled with the Coriolis parameter (the rightmost term in eq. (2.2)) contributes to the magnitude of the same mechanism (β-effect in the present problem) which controls the band of scales insensitive to a variation of resolution.

5. Conclusions

Recent developments in enhanced sophistication of regional models focuses attention on the question of potential mesoscale predictability. Statistical-dynamical considerations lead to a pessimistic conclusion on predictability in the mesoscale region (Anthes et al., 1985). Closer observational studies of the mesoscale phenomena and the forcing mechanisms involved suggest higher determination of those scales which need to be studied by more adequate means. Direct utilization of operational models in predictability studies reveals large case dependence due to specific initial and lateral boundary conditions. While such studies are the object of intensive research, we have approached the question from a scale truncation viewpoint. In order to reduce the number of degrees of freedom required by operational regional models, we considered the simplest possible high resolution models which still contain the major characteristics of nonlinear flows. Experimentation of this type can provide irreplaceable information to complement results from complex models and aid us in our understanding of atmospheric nonlinear dynamics.

In order to establish the dependence of numerical nonlinear model integrations on the truncation of mesoscale energy variance, 24-h predictions over a wide range of modes are compared. Two models were utilized to simulate barotropic channel flow in the middle latitudes. Their spectral formulation enabled the representation of grid length variations, typical for regional models, as spectral truncation rather than grid-point truncation. Consequently, results were obtained and compared in two-dimensional wavenumber space. The number of modes was varied from 21 to 171 in the zonal direction and from 10 to 85 in the meridional direction. Integrations were performed with three data sets which represent various energy distributions in the mesoscale range. A k^{-3} power law was assumed for synoptic wavelengths and a $k^{-5/3}$ power law was assumed for mesoscale wavelengths shorter than 800 km.

Much of what we have observed and discussed is summarized in Fig. 13. On that figure, we plotted the absolute value of Δ_m^n which is defined to be the 24-h forecast difference between two integrations for each wavelength in the model scale region. Integrations which are compared are for a fixed truncation range and for a truncation range which includes twice as many scales. Thus, for example, a wave amplitude in the M scale region will be compared in the figure for an integration which terminates at the M scales with one which terminates at the F scales. In all these comparisons the initial energy amplitude for the integrations have zero values in the expanded scale region.

Let us assume that a difference in amplitude of any wave component as depicted on Fig. 13 indicates that the expanded grid provides an improved forecast. We first note from curve (a) that the improvement is substantial for the longest C modes, and gradually reduces as the wavelength is decreased. As one proceeds to the shorter M modes, the improvement in forecast seems unaffected by scale. Indeed in the domain of wavelengths $150 > L > 75$ km, the forecast improvement noted by the addition of higher resolution seems not to be scale dependent. This observation is modified as one proceeds to still shorter scales. For scales $L < 75$ km, as one proceeds to the shortest scales, the difference in forecast grows, suggesting that in the short-scale domain (typical scales of mesoscale convective systems), the additional resolution is of forecast advantage.

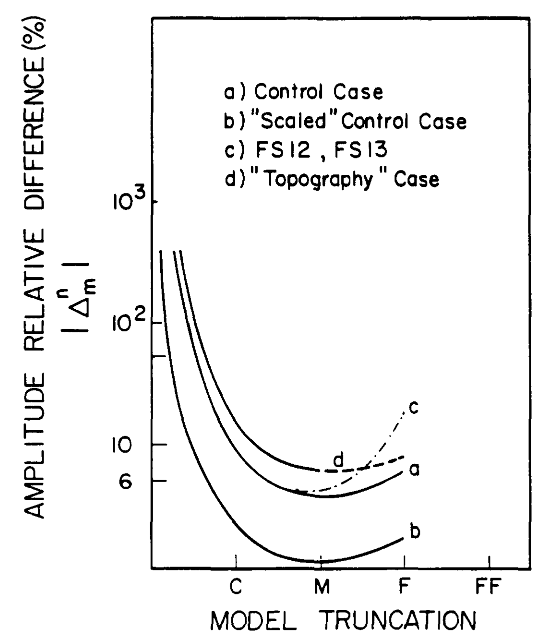

Fig. 13. 24-h forecast difference between two integrations for each wavelength in the model scale region summarized from all nine experiments. Integrations which are compared are for a fixed truncation range and for a truncation range which includes twice as many scales.

The magnitude of the difference or improvement is dependent on the choice of initial conditions. Thus, we see that the Control Case (FS00) shows less sensitivity to resolution over the entire scale range than do the experiments with FS12 and FS13 data (see curves (a) and (c) in Fig. 13). To indicate the senstivity of the process (varying resolution) we modify our BVE model by reducing the magnitude of the Coriolis parameter by two orders of magnitude, and define the integration with this condition as the "scaled" control case. The results clearly show (diagram curve (b)) that for the scales of interest in the mesoscale, the effects from the "scaled" experiment are virtually insensitive to model resolution.

The influence of the perturbation at the lower boundary is illustrated by curve (d) in Fig. 13. Integrations with BVE model indicate increased prediction sensitivity to model resolution for the

C modes. The inclusion of the forcing function (eq. (2.2)) resulted in an additional rotational term in the vorticity equation when compared with the BVE (eq. (2.1)). This term also demonstrates a rôle of scale-lock (as opposed to the "scaled" control case, curve (b)) caused by the contribution of a one order of magnitude larger rotational term coupled with the Coriolis parameter. The large magnitude of this term probably resulted in the expansion of the scale lock which forces the shortest (F) modes to become insensitive to changes in resolution (extension of line (d) in dashed pattern).

When these conclusions are projected onto results of nested grid models or limited-area models embedded in the large-scale models they could be interpreted as follows. The predictability of subsynoptic waves (in this particular case mesoscales with wavelengths between 400 km and 100 km) would benefit from finer M resolution in the sense that the nonlinear interactions of a higher number of modes would "relax" integrations and fictitious accumulation of energy in those modes. At the same time further increase of resolution (F or FF truncation) would not have additional impact on those modes as long as their propagation is controlled by large scale tendencies prescribed at the lateral boundaries. The irrelevance of the short scale perturbation at the lateral boundaries (described by the FS12 and FS13 data) indicates that one can expect that imperfect inner boundaries may not significantly alter predictions of the C wavelengths, at least not on the 24-h time scale. The impact of all these effects on the predictability of subsynoptic scales needs to be investigated by the more realistic model integrations, but based upon our findings we would expect it to be compensated sufficiently well by the model diffusion parameterization when correct large-scale tendencies are provided. In the latter case, the resolution increase of both the model and observations would not be expected to show apparent improvement.

However, the sensitivity of the shortest mesoscales considered, i.e., wavelengths between 50 km and 100 km, shows that one may not expect the predictability of these scales to be solely controlled by the large-scale flow as are the meso-α scales. The lack of fine resolution initial information on the lateral boundaries and insufficient domain resolution are crucial for these scales. Their sensitivity to initial information, as illustrated by Fig. 9, indicates that predictability of these scales can be improperly driven by the model diffusion parameterization even if the large-scale flow is included correctly.

To summarize briefly, we expect that the prediction of meso-α and longer -β scales by interactive limited-area models is mostly controlled by the large scale tendencies and the resolution of finer grid. However, the predictability of the shortest meso-β scales may crucially depend upon data resolution and model diffusion since they are not controlled by the large scales.

These conclusions are only tentative but may assist in the explanation of the results of studies which employ realistic models (e.g., Leslie et al. (1981), Errico and Baumhefner (1987)). Many mesoscale phenomena on temporal and spatial scales studied herein are baroclinic in nature, and the divergent component of the flow may play as significant a rôle as the rotational part (especially for the shortest mesoscales). Thus it is necessary to extend present findings with studies using at least a minimal baroclinic model (i.e., a two-layer model) where the number of degrees of freedom can be controlled in a similar fashion. Gradual addition of the divergent part of the wind, diffusion parameterization, and realistic data to models of the type presented herein should provide useful information for solving those problems related to model and data resolution in mesoscale numerical models, and should be pursued.

6. Acknowledgements

The authors thank J. Tribbia and D. Baumhefner for valuable suggestions and discussion. We thank Barbara Gilkes for careful preparation of the manuscript and Giovanni Soto for preparation of the figures, both from the Purdue University. This research has been supported by the National Science Foundation under Grants ATM82-12201 and ATM85-21374 to the University of Maryland. Additional support was provided by NOAA/NMC through Grant NA84AA-H00026 to the University of Maryland. Computer time and assistance was provided by the University of Maryland and NASA/GSFC, Greenbelt, MD, USA.

REFERENCES

Anthes, R. A. 1983. Regional models of the atmosphere in middle latitudes. *Mon. Wea. Rev. 111*, 1306–1335.

Anthes, R. A., Kuo, Y.-H., Baumhefner, D. P., Errico, R. M. and Bettge, T. W. 1985. Predictability of mesoscale atmospheric motions. Contributions to "Issues in Atmospheric and Oceanic Modeling". Part II, *Advances in Geophysics 28*, 159–202.

Baer, F. 1964. Integration with the spectral vorticity equation. *J. Atmos. Sci. 21*, 260–276.

Baer, F. and Alyea, F. M. 1971. Effects of spectral truncation on general circulation and long-range prediction. *J. Atmos. Sci. 28*, No. 4, 457–480.

Charney, J. G. 1971. Geostrophic turbulence. *J. Atmos. Sci. 28*, 1087–1095.

Errico, R. and Baumhefner, D. P. 1987. Predictability experiments using a high-resolution limited-area model. *Mon. Wea. Rev. 115*, No. 2, 488–504.

Fjørtoft, R. 1953. On the changes in the spectral distribution of kinetic energy for two-dimensional nondivergent flow. *Tellus 5*, 225–230.

Gage, K. S. 1979. Evidence for $k^{-5/3}$ law inertial range in mesoscale two-dimensional turbulence. *J. Atmos. Sci. 36*, 1950–1954.

Gottlieb, D. and Orszag, S. A. 1977. *Numerical analysis of spectral methods. Theory and applications.* Society for Industry and Applied Mathematics, Philadelphia, USA. 172 pp.

Leith, C. E. 1971. Atmospheric predictability and two-dimensional turbulence. *J. Atmos. Sci. 28*, No. 2, 145–161.

Leith, C. E. and Kraichnan, R. H. 1972. Predictability of turbulent flows. *J. Atmos. Sci. 29*, 1041–1058.

Leslie, L. M., Mills, G. A. and Gauntlett, D. J. 1981. The impact of FGGE data coverage and improved numerical techniques in numerical weather prediction in the Australian region. *Q. J. R. Meteorol. Soc. 197*, 629–642.

Lilly, D. K. and Petersen, E. L. 1983. Aircraft measurements of atmospheric kinetic energy spectra. *Tellus 35A*, 379–382.

Lorenz, E. N. 1969. The predictability of a flow which possesses many scales of motion. *Tellus 21*, 289–307.

Machenhauer, B. 1979. The Spectral Method. In *Numerical methods used in atmospheric models*, Vol. II, GARP Publication Series No. 17, WMO, Geneva, Switzerland, 499 pp.

Meriless, P. E. 1972. Truncation error in a spectral model. *Atmosphere 10*, No. 1, 1–9.

Orlanski, I. 1975. A rational subdivision of scales for atmospheric processes. *Bull. Amer. Meteor. Soc. 56*, 527–530.

Orszag, S. A. 1970. Transform method for calculation of vector-coupled sums: Application to the spectral form of vorticity equation. *J. Atmos. Sci. 27*, 890–895.

Orszag, S. A. 1971. On the elimination of aliasing in finite-difference schemes by filtering high-wave-number components. *J. Atmos. Sci. 28*, 1074.